Infrared Small-Target Detection Using Multiscale Gray Difference Weighted Image Entropy

HE DENG
Chinese Academy of Sciences
and
Central China Normal University
Wuhan, China

XIANPING SUN
MAILI LIU
CHAOHUI YE
XIN ZHOU
Chinese Academy of Sciences
Wuhan, China

We propose an effective small-target detection approach based on weighted image entropy. The approach weights the local entropy measure by the multiscale grayscale difference followed by an adaptive threshold operation, which aims to improve the signal-to-noise ratio for cases in which jamming objects in the scene have similar thermal intensity measure with respect to the background as small target. The detection capability of the proposed approach has been validated on six real sequences, and the results demonstrate its significance and improvement.

Manuscript received November 21, 2014; revised April 9, 2015; released for publication July 9, 2015.

DOI. No. 10.1109/TAES.2015.140878.

Refereeing of this contribution was handled by H. Kwon.

This work was supported by the Natural Science Foundation of China (81227902, 61471355), and the China Postdoctoral Science Foundation funded project (2014M560636, 2015T80856).

Author's address: H. Deng, X. Sun, M. Liu, C. Ye, X. Zhou, State Key Laboratory of Magnetic Resonance and Atomic and Molecular Physics, National Center for Magnetic Resonance in Wuhan, Wuhan Institute of Physics and Mathematics, Chinese Academy of Sciences, 30 West Xiaohongshan, Wuhan 430071, China, E-mail: (xinzhou@wipm.ac.cn); H. Deng, Department of Information Technology, Central China Normal University, 152 Luoyu Road, Wuhan 430079, China.

I. INTRODUCTION

Compared with radar systems, infrared (IR) search and tracking (IRST) systems have some advantages, such as simple structure, high resolution, good concealment, and strong antijamming capability, and they have all-weather and strong smoke penetration abilities in comparison to visible light systems. IR small-target detection is one of the crucial techniques in IRST systems because the precise detection determines both the effective range and the complexity of the whole IRST system [1]. Therefore, many researchers have paid much attention to the study of IR small-target detection, especially to those images that are against complex and noisy backgrounds [2–5].

There exist a number of techniques for detecting small targets, which can be roughly categorized into two groups: track-before-detect (TBD) techniques [2] and detect-before-track (DBT) techniques [3]. The TBD techniques usually process a number of frames to estimate targets, while necessitating some prior knowledge about the field (shape and velocity) of the target [1]. The classical methods are three-dimensonally (3D) matched (directional) filter [6], 3D double directional filter [7], and improved 3D directional filter [8]. The DBT techniques are powerful owing to their shorter computation time and lesser memory requirement. Because of the long imaging distance, small targets are small in size and weak in intensity, and they have no prior knowledge (e.g., size, shape, and texture) [1]. Thus, the TBD techniques are not generally adopted in practical detection devices, while the DBT techniques are more appropriate for the space detecting and tracking. However, small targets usually submerge in the complex and noisy background clutter, resulting in a low signal-to-noise ratio (SNR) of the image. This produces great difficulties in the detection of IR targets. Although many research efforts have been focused on the detection of IR small targets against complex and noisy backgrounds in past decades, it still remains an open problem [1, 3–5].

IR small-target detection is usually in accord with two assumptions [4]. The first is that backgrounds have the correlation in the spatial domain and the stability in the time domain, and they occupy the low-frequency portion of IR images in the frequency domain. The second assumption is that targets are unrelated to the background in spatial domain, and they dominate the high-frequency portion of IR images in frequency domain. Depending on whether the focus is on the backgrounds, the targets, or both of them results in different small-target detection methods. They are generally divided into three categories: time-domain methods, spatial-domain methods, and transform-domain methods. Time-domain methods are mainly used to suppress backgrounds with the property of the short-time stationarity, such as the finite or infinite impulse response filter and the space-time maximum likelihood algorithms [9]. Spatial-domain methods have good real-time performance, e.g., the median filter, max-mean and max-median filter [10], and the top-hat

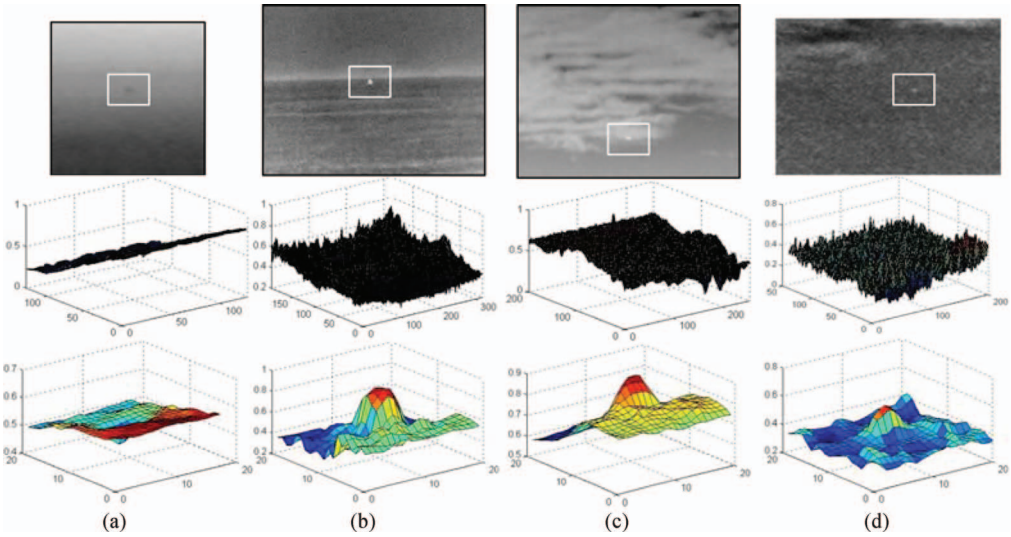

Fig. 1. Representative small targets (upper) against different backgrounds, corresponding 3D surfaces (middle) of whole images (normalized), and corresponding 3D surfaces (lower) of selected local regions (normalized). (a) Dim airplane target against sea-sky background. (b) Bright ship target against sea-sky background with heavy noise. (c) Bright airplane against sky cloud background. (d) Dim airplane target against sky background with heavy noise.

filter [3]. The top-hat filtering algorithm requires prior knowledge about the image, and it is sensitive to noise [1, 11]. Transform-domain methods (e.g., the Butterworth high-pass filter [12] and the wavelet transform [13]) are rooted from Fourier transform, and they are restricted by the Heisenberg uncertainty principle. The restriction hinders these algorithms simultaneously, achieving high accuracy in both the time domain and frequency domain [14]. In addition, classification-based methods are useful for removing various clutter points [15], such as the nearest-neighbor classifier [16], learning-based neural network [17], manifold learning [18], and support vector machine [19]. There are still many other algorithms for IR small-target detection, such as methods based on statistical regression [20], empirical mode decomposition [21], a trifeature-based detector [22], and biological vision [23, 24]. As a consequence, the study of those detection algorithms with good traits of simple structure, good filtering effect, and strong robustness plays the key role in the development of IR small-target detection.

Generally, a small-target IR image model I can be assumed as [1, 20]

$$I(x, y) = I_{\text{target}}(x, y) + I_{\text{back}}(x, y) + I_n(x, y), \quad (1)$$

where I_{target}, I_{back}, I_n and (x,y) are the target image, the background image, the random noise image and the pixel location, respectively. The target shapes are generally considered as rough circles without anisotropy and prevailing orientations [1, 25]. Thus, a small target may be modeled by using a two dimensional Gaussian function [26]. I_n is usually assumed as Gaussian white noise. Under these assumptions, the SNR of a small-target IR image is formulated as follows [27]:

$$SNR = (I_{\max} - I_{\text{mean}})/\sigma, \quad (2)$$

where $I_{\max}$, I_{mean}, and σ are the maximum gray value, the mean value, and the standard deviation of the image I, respectively.

According to the concept of a small target defined by SPIE from the perspective of imaging, a small target has a total spatial extent of less than 80 pixels [28]. Fig. 1 represents four IR small-target images against different backgrounds (these samples come from the same sequences used in the experiments). The target sizes range from 2×2 to 8×8 pixels, and the intensities vary from dim to bright due to different imaging distances, environments, and noise intensities. According to (2), the SNR values of Figs. 1a–1d are 1.7257, 5.9441, 3.4834, and 6.1844, respectively. Because the emergence of a small target causes considerable changes of image texture in a local region rather than the whole image plane (see Fig. 1, where the size of the local region is chosen as 20×20), some operators that represent the local mutation because of the appearance of a small target have been applied to detect small targets, such as the local entropy operator [14], the local mutation weighted information (LMWIE) [27], the weighted self-information map [4], the fast local reverse entropy [28], and the average gray absolute difference maximum map (AGADM) [29]. In addition, inspired by the human visual mechanism, a scale invariant small-target detection method has been proposed [11]. A sparse ring representation is an effective graphical structure that can describe the local difference between the background and targets [5].

The authors of [18, 29] pointed out that a small target had a signature of discontinuity with its neighboring areas and concentrated in a relatively small region that could be viewed as a homogeneous compact region, and the background was consistent with its neighboring areas. This discontinuity was essentially involved in determining the property of average gray difference based on the

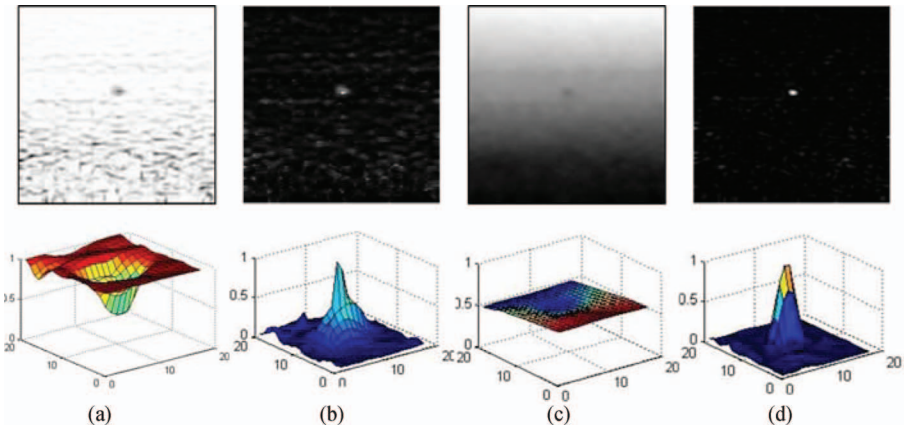

Fig. 2. Filtered results (upper) and corresponding 3D surfaces (lower) of local selected regions obtained through different filtering methods (normalized). (a) Local entropy operator. (b) LMWIE. (c) AGADM. (d) Multiscale gray difference.

neighboring pixels [29]. Consequently, we conceive some local measure that determines the dissimilarity of regions in the image from their surrounding areas. After the dissimilarity measure, the local region, whose dissimilarity is larger than a given threshold in some scale, may be a position in which the small target emerges. With these considerations in mind, a small-target detection method based on the novel weighted image entropy (NWIE) has been designed in this paper. It is inspired by the concept of multiscale gray difference and local entropy operator, and it aims to process low SNR small-target images against complex backgrounds.

Our method has two advantages. The first is the inclusion of a multiscale gray difference measure, which intends to measure the dissimilarity of regions in the image from their surrounding areas and subsequent weighting of the local image entropy measure of the same region. It can improve the SNR for cases in which jamming objects (e.g., edge of clouds) in the scene have a similar thermal intensity measure with respect to (wrt) the background as small target, and it can enhance the target and suppress background clutter simultaneously. The second advantage is that the designed small-target IR detection algorithm can effectively process low SNR small-target images against complex and noisy backgrounds. By applying this method on extensive real images with different clutters and noise backgrounds, we demonstrate that the designed method not only works more robustly for detecting different target types and target movements but also has better detection performance in comparison with the well-known baseline methods. In particular, it can significantly improve the SNR of the image.

The organization of the remainder of this paper is as follows: In Section II, we review the related work. In Section III, we explain the small-target detection method based on the NWIE in detail. In Section IV, we give real extensive data experimental results and discussions. Conclusions and perspectives are given in Section V.

II. RELATED WORK

According to [23], a small target occupies less than 0.15% of the input image with a matrix size of 256×256. Thus, the emergence of the target produces a tiny mutation of the whole image texture characteristics, but in the local area around the target, the target causes great changes to the local region texture. Some local operators (e.g., the local entropy operator and the local gray difference measure) are explored to further highlight the targets and suppress the complex background as much as possible. Local operators belong to the spatial-domain algorithm, which is easy to be realized.

A. Local Entropy

Information entropy or Shannon entropy tells how much information there is in an information source, and it can represent the global characteristics of an information source in an average sense. Similar to the information entropy, an image entropy is constructed based on the image histogram [14], and it is an efficient approach to illustrate the complex degrees of grey value distribution upon an image [30, 31]. For an image I whose size is $M \times N$ and grey level is L, its entropy is

$$E_1 = -\sum_{i=0}^{L-1} p_i \cdot \log_2 p_i, \quad p_i = {}^{n_i}\!/_{M \times N}, \qquad (3)$$

where p_i is the probability density function (PDF) of the ith gray level, and n_i is the number of pixels of the ith gray level.

Although the image entropy has statistical significance, it neglects the texture and frequency information of an image [32]. Thus, the local entropy operator is restricted in a local window whose size is $M_k \times N_k$, and it can represent the information content contained in the window. When a small target appears in an IR image, the texture characteristic in the local area around the target is destructed, which produces the change of the local entropy. For Fig. 1a, the filtered result obtained through the local entropy operator (the size of local window is 5×5) is shown in Fig. 2a. According to the

maximum entropy principle, the entropy value is greater in homogeneous regions than that in inhomogeneous ones. To some extent, the local entropy operator can be adopted to enhance IR small targets against complex backgrounds.

B. Weighted Local Entropy

Because a small target normally appears in the form of a high grey value in the IR images, the LMWIE is explored to emphasize the contribution of high grey value components to the information entropy of an image [27]. Assume that $I(x,y)$ is the gray value at the point (x,y), and its neighborhood (local window) includes m kinds of gray values $I_1, I_2, \ldots, I_m$. Then, the LMWIE of $I(x,y)$ can be expressed as

$$E_2(x, y) = -\sum_{i=1}^{m} (I_i - I(x, y))^2 p_{I_i} \log_2 p_{I_i}, \qquad (4)$$

where $p_{I_1}, p_{I_2}, \ldots, p_{I_m}$ are PDFs of each gray value. Equation (4) represents the information of weighted local entropy contained in the local window. The filtered result based on LMWIE is shown in Fig. 2b, where the SNR is improved (the size of local window is 5×5, and the SNR of the filtered result is 19.3830).

C. Average Gray Absolute Difference

The IR small-target detection aims to detect small objects from natural scenes and to derive the criteria of distinguishing objects from natural scenes, and it, in essence, involves determining the property of the dissimilarity based on the neighboring pixels in natural scenes [29]. Then, the concept of the AGADM is presented to measure that dissimilarity, which is formulated as follows [29]:

$$E_3(x, y) = \max_{\forall \Theta} \left(\Delta D \left| \Delta D = \left| \frac{1}{N_\Theta} \sum_{(x,y)\in\Theta} I(x, y) - \frac{1}{N_\Omega} \sum_{(x,y)\in\Omega} I(x, y) \right| \right), \qquad (5)$$

where the set Θ denotes the pixels contained in the internal window, the set Ω denotes the pixels contained between the internal window and the external window, $I(x,y)$ denotes the gray value at point (x,y), and N_Θ and N_Ω are the number of pixels contained in sets Θ and Ω, respectively. For Fig. 1a, the filtered result obtained through the AGADM (the size of local window is 9×9) is shown in Fig. 2c. The filtered result based on the AGADM is similar to that of the smoothing method for this image case.

III. TARGET DETECTION BASED ON NWIE

In this section, we introduce a new IR small-target detection scheme that weights the local entropy measure of a region by the multiscale gray difference to improve the SNR and, subsequently, adopts an adaptive threshold for detecting targets from the filtered images. It is good at improving small-target detection in IR images.

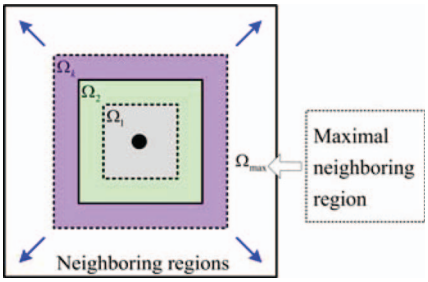

Fig. 3. Pixel point and its neighboring areas.

A. Multiscale Gray Difference

Human recognition of a small target from a natural scene is based on the target region having a conspicuous discontinuity with its neighboring areas and concentrating in a relatively small area [23, 29]. The target region is usually treated as a homogeneous compact area, and the scene is consistent with its neighboring areas. Thus, the most dissimilar point, based on specific metric in the scene, is considered as a target.

The concepts of gray difference and multiscale gray difference are presented to measure the dissimilarity of the target region from its surrounding areas (see Fig. 3). For an image I with L grey levels, the kth gray difference at the point $(x,y$; i.e., the dark point in Fig. 3) can be formulated as follows:

$$D_k(x, y) = \left| \frac{1}{N_{\Omega_k}} \sum_{(s,t)\in\Omega_k} I(s, t) - \frac{1}{N_{\Omega_{\max}}} \sum_{(p,q)\in\Omega_{\max}} I(p, q) \right|^2, \qquad (6)$$

where $k = 1, 2, \ldots, K$. The sets Ω_ks denote the pixels contained in the internal windows (i.e., the neighboring areas), the set $\Omega_{\max}$ denotes the pixels contained in the maximal neighboring area, $I(s,t)$ and $I(p,q)$ denote the gray value at point in Ω_k and $\Omega_{\max}$, N_{Ω_k} and $N_{\Omega_{\max}}$ are the number of pixels contained in sets Ω_k and $\Omega_{\max}$, and K is the number of the neighboring areas, respectively.

The method to compute the gray difference is shown in Algorithm 1, where l_{max} is a positive odd number. The size of the kth neighboring area is $(2k + 1) \times (2k + 1)$, $k = 1, 2, \ldots, K$, $K = 0.5(l_{max} - 1)$. For each pixel point in a given scale, we can obtain a set of the gray difference in this way.

ALGORITHM 1 Gray difference computation.

INPUT Examined image patch centered at point (x,y).
OUTPUT $D_k(x,y)$.
1) Set the size of the maximal neighboring area $\Omega_{\max}$, i.e., $l_{max} \times l_{max}$.
2) Obtain the set of neighboring areas at point (x,y)
$$\{\Omega_k | \Omega_k \subseteq \Omega_{\max}, k \in \{1, 2, \ldots, K\}\}.$$
3) **for** $k = 1,2,\ldots,K$ **do**
$$D_k(x, y) = \left| \frac{1}{N_{\Omega_k}} \sum_{(s,t)\in\Omega_k} I(s, t) - \frac{1}{N_{\Omega_{\max}}} \sum_{(p,q)\in\Omega_{\max}} I(p, q) \right|^2.$$
4) **end for**.

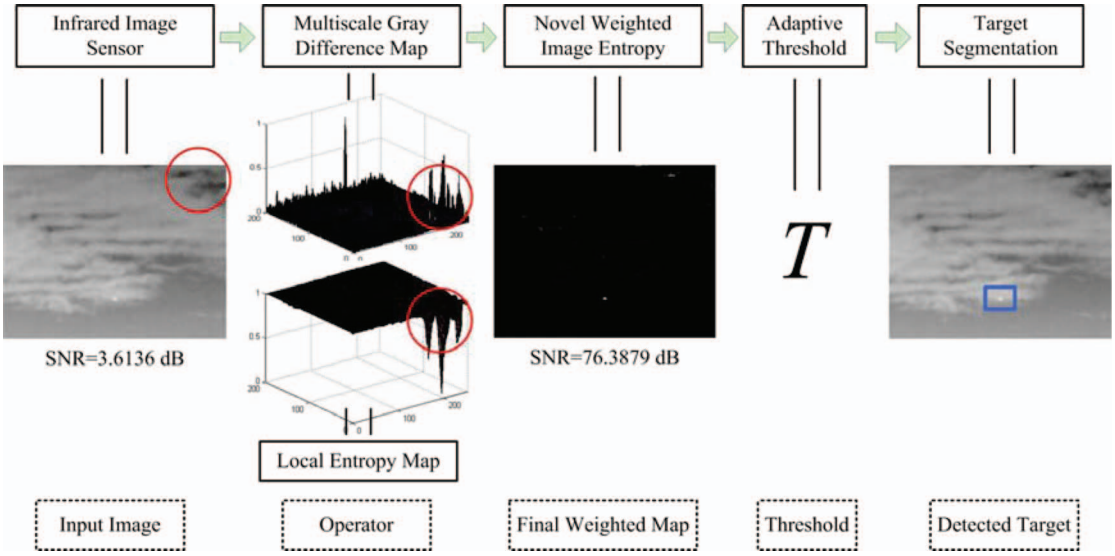

Fig. 4. Overview of proposed small-target detection system.

Then, the multiscale gray difference at the point (x,y) is

$$D(x, y) = \max\{D_1(x, y), D_2(x, y), \ldots, D_K(x, y)\}. \quad (7)$$

When the local window in (7) moves within an image from left to right and from top to bottom, the matrix of multiscale gray difference will be obtained, where each element represents the information of maximal gray difference contained in the local window. For an image I whose size is $M \times N$, the computation of the multiscale gray difference is descried in Algorithm 2.

ALGORITHM 2 Multiscale gray difference.

INPUT Given frame.
OUTPUT D.
1) Enough scales of the window are given.
2) **for** $x = 1{:}M$ **do**.
3) **for** $y = 1{:}N$ **do**.
Compute $D_k(x,y)$ according to Algorithm 1, $k = 1,2, \ldots, K$.
4) $D(x, y) = \max\{D_1(x, y), D_2(x, y), \ldots, D_K(x, y)\}$.
5) Replace the value of the central pixel with the $D(x,y)$.
6) **end for**.
7) **end for**.

B. NWIE

The filtered result of Fig. 1a based on the multiscale gray difference is shown in Fig. 2d, which suggests that the target is well enhanced and the background is well suppressed (the size of the maximal neighboring area is chosen as 7×7). According to (2), the SNR of Fig. 2d is 33.9011, which indicates that the multiscale gray difference is suitable to greatly improve the SNR of the small-target IR image. However, for IR images against complex sea-sky or sky backgrounds, the edge of the clouds (i.e., the border area between the cloud and the sky) has a similar thermal intensity measure as a small target (e.g., the area marked by red circles in Fig. 4), which greatly affects the performance of the multiscale gray difference. Therefore, a NWIE that integrated the multiscale gray difference with the local entropy operator is proposed to offset this effect, improving both the adaptability and the robustness of the multiscale gray difference.

Assume that an image I is with the size of $M \times N$, the local entropy operator is expressed as follows [14]:

$$E_4(x, y) = -\sum_{i=x-(m-1)/2}^{x+(m-1)/2} \sum_{j=y-(n-1)/2}^{y+(n-1)/2} p_{ij} \log_2 p_{ij}$$

$$\text{with } p_{ij} = I(i, j) \Big/ \sum_{s=x-(m-1)/2}^{x+(m-1)/2} \sum_{t=y-(n-1)/2}^{y+(n-1)/2} I(s, t), \quad (8)$$

where $m \times n$ is the size of the neighboring area centered at the pixel point (x,y) and m and n are odd integer numbers, respectively. The method to compute the local entropy operator is shown in Algorithm 3.

ALGORITHM 3 Local entropy operator.

INPUT Given frame.
OUTPUT E_4.
1) The size of the neighboring area at each pixel point is given.
2) **for** $x = 1{:}M$ **do**.
3) **for** $y = 1{:}N$ **do**.
$p_{ij} = I(i, j) \Big/ \sum_{s=x-(m-1)/2}^{x+(m-1)/2} \sum_{t=y-(n-1)/2}^{y+(n-1)/2} I(s, t)$, $I = x - (m-1)/2 : x + (m-1)/2$, $j = y - (n-1)/2 : y + (n-1)/2$.
4) $E_4(x, y) = -\sum_{i=x-(m-1)/2}^{x+(m-1)/2} \sum_{j=y-(n-1)/2}^{y+(n-1)/2} p_{ij} \log_2 p_{ij}$.
5) Replace the value of the central pixel with the $E_4(x,y)$.
6) **end for**.
7) **end for**.

Thus, the NWIE can be obtained through the following expression:

$$\begin{aligned} &NWIE(x, y) \\ &= -\sum_{i=x-(m-1)/2}^{x+(m-1)/2} \sum_{j=y-(n-1)/2}^{y+(n-1)/2} D(x, y) \cdot p_{ij} \log_2 p_{ij} \\ &= -D(x, y) \cdot \sum_{i=x-(m-1)/2}^{x+(m-1)/2} \sum_{j=y-(n-1)/2}^{y+(n-1)/2} p_{ij} \log_2 p_{ij} \\ &= D(x, y) \odot E_4(x, y), \end{aligned} \tag{9}$$

where $D(x,y)$ and $E_4(x,y)$ denote the multiscale gray difference and the local entropy operator at the point (x,y), respectively. The computation of NWIE is explained in Algorithm 4.

ALGORITHM 4 The NWIE computation.

INPUT Given frame.
OUTPUT *NWIE*.
1) The size of the maximal neighboring area at each pixel point is given for the computation of the multiscale gray difference.
2) The size of the neighboring area at each pixel point is given for the computation of the local entropy operator.
3) **for** $x = 1{:}M$ **do**.
4) **for** $y = 1{:}N$ **do**.
Compute $D(x,y)$ according to Algorithm 2.
5) Compute $E_4(x,y)$ according to Algorithm 3.
6) $NWIE(x, y) = D(x, y) \odot E_4(x, y)$.
7) Replace the value of the central pixel with the $nWE(x,y)$.
8) **end for**.
9) **end for**.

C. NWIE-Based Small-Target Detection Method

The NWIE map enlarges the discontinuity of the target region from its neighboring areas, and the target region concentrates on a relatively small-bright homogeneous compact area (see Fig. 4). Consequently, the NWIE-based small-target detection method can be described in Algorithm 5, where m, σ, $\mathrm{NWIE}_{\max}$, and c are the mean, the standard deviation, the maximum of the final weighted map, and the positive constant, respectively. The user can choose parameter c according to the practical design requirements. In our experiments, c is selected from the interval [0.5, 0.65]. To intuitively show the proposed method, a target detection system is given in Fig. 4.

ALGORITHM 5 Target detection method.

INPUT One frame.
OUTPUT Target position.
1) Obtain NWIE according to Algorithm 4.
2) Compute the threshold according to

$$T = c \cdot SNR \cdot \sigma + m, \quad SNR = (NWIE_{\max} - m)/\sigma. \tag{10}$$

3) Segment targets from the background according to T.

D. Detection Ability Analysis

From the definition, we can find that the multiscale gray difference can measure the local mutation when a small target appears. Let (x_0,y_0) be the center pixel of the target, and we consider the following expression:

$$\tilde{D}_k^o(x_0, y_0) = \left| \frac{1}{N_{\Omega_k}} \sum_{(s,t)\in\Omega_k} I(s,t) - \frac{1}{N_{\Omega_{\max}}} \sum_{(p,q)\in\Omega_{\max}} I(p,q) \right|^2 \Big/ |\tilde{d}^o(x_0, y_0)|^2, \tag{11}$$

where

$$\tilde{d}^o(x_0, y_0) = \max\left\{\tilde{d}_1(x_0, y_0), \tilde{d}_2(x_0, y_0), \ldots, \tilde{d}_K(x_0, y_0)\right\} \tag{12}$$

and

$$\overset{\frown}{d}^o(x_0, y_0) = \min\left\{\tilde{d}_1(x_0, y_0), \tilde{d}_2(x_0, y_0), \ldots, \tilde{d}_K(x_0, y_0)\right\} \tag{13}$$

where

$$\tilde{d}_k(x_0, y_0) = \frac{1}{N_{\Omega_k}} \sum_{(s,t)\in\Omega_k} I(s,t), \quad k = 1, 2, \ldots, K. \tag{14}$$

Because a small target concentrates in a homogeneous compact area and has a signature of discontinuity with its neighboring areas [23, 29], the multiscale gray difference of the target region in the image from their surrounding areas is conspicuous. For a bright small target, it can be found that $\tilde{d}_k(x_o, y_o) \geq \tilde{d}_{k+1}(x_o, y_o)$, $k = 1, 2, \ldots, K-1$. Then,

$$\begin{aligned} \tilde{D}^o(x_0, y_0) &= \max\left\{\tilde{D}_1^o(x_0, y_0), \tilde{D}_2^o(x_0, y_0), \ldots, \tilde{D}_K^o(x_0, y_0)\right\} \\ &= |1 - \tilde{d}_K(x_0, y_0)/\tilde{d}^o(x_0, y_0)|^2 \in (0, 1). \end{aligned} \tag{15}$$

As for a dark small target, we find that $\tilde{d}_k(x_o, y_o) \leq \tilde{d}_{k+1}(x_o, y_o)$. Then $\tilde{D}^o(x_0, y_0) = |1 - \overset{\frown}{d}^o(x_0, y_0)/\tilde{d}^o(x_0, y_0)|^2 \in (0, 1)$. If the size of maximal neighboring area is selected appropriately, the value of $\tilde{D}^o(x_o, y_o)$ will be near to 1.

On the contrary, if the current location is the background, the local mutation will be small because the background has the correlation in the spatial domain and the stability in the time domain [4]. In a local background region, the following relationship is tenable:

$$\tilde{d}_k(x_o, y_o) \approx \tilde{d}_{k+1}(x_o, y_o), \quad k = 1, 2, \ldots, K-1, \tag{16}$$

Then,

$$\tilde{D}^b(x_0, y_0) \approx 0. \tag{17}$$

Equations (11)–(17) suggest that the multiscale gray difference in the target region is higher than that in the background region. In this way, the target can be enhanced, and the background can be suppressed. Thus, we can use the multiscale gray difference map to detect the target. In addition, the local entropy operator and its variations have been presented to effectively measure the local mutation due to the appearance of a small target [14, 27, 28]. Consequently, the weighted image entropy integrating the multiscale gray difference and the local

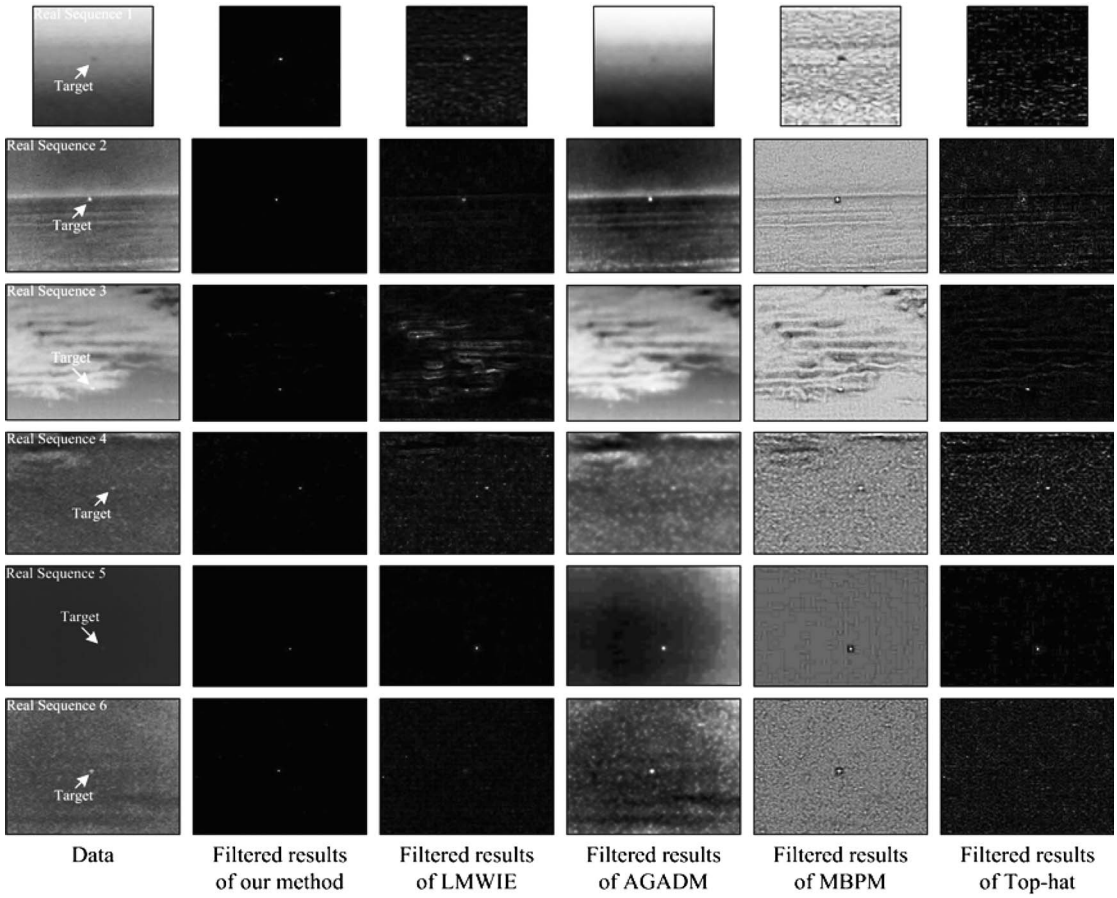

Fig. 5. Representative images of six real infrared image sequences and corresponding processed results obtained through different methods.

entropy operator considers the problems of target enhancement and background suppression simultaneously, and the weighted image entropy map can work well for different small-target IR images.

IV. EXPERIMENTS

In this section, we first introduce the evaluation metrics, the baseline methods and the data for comparison. Then, we use real IR image sequences to demonstrate the effectiveness and practicality of the proposed method. The experiments were conducted on a computer with 4-GB random access memory and Intel Core 2 Duo CPU E7500, 2.93GHz processor, and the code was implemented in MATLAB.

A. Metrics, Baseline Methods, and Data

The probability of detection (Pd) and the false alarm rate (Fa) are the most important metrics of evaluating the detection performance of small-target detection methods [1, 25]. Pd represents the probability of targets detected in multiframes in which small targets truly exist, while Fa denotes the false alarm rate of targets in multiframes in which targets do not exist. Pd and Fa are described as follows:

$$Pd = N_{detect} \big/ N_{actual},\ Fa = M_{false} \big/ M_{total}, \qquad (18)$$

where N_{detect}, N_{actual}, M_{false}, and M_{total} represent the number of detected true targets, the number of actual targets, the number of detected false targets, and the number of images, respectively.

SNR and SNR gain (SNRG) can also be used to describe the difficulty degree of small-target detection. As a general rule, the higher both the SNR and the SNRG of a small-target image are, the easier targets can be detected. In this paper, SNRG is defined as follows:

$$SNRG = 20 \times \log_{10}\left(SNR_O \big/ SNR_I\right), \qquad (19)$$

where SNR_O and SNR_I denote the SNR of the original image and the SNR of the filtered image, respectively.

Because our method depends on the local mutation of IR images, we choose local descriptors, e.g., LMWIE [27] and AGADM [29] as two baseline methods. Moreover, the top-hat [3, 33, 34] filtering method and the maximum background prediction model (MBPM) method [35] are also chosen as the baseline methods in this paper.

We use six real IR image sequences with low SNR to compare the proposed methods with the baseline methods. The gray value ranges of the IR images are normalized to uint8. The first column in Fig. 5 has representative images of six real IR sequences denoted as Real Sequences 1 to 6,

TABLE I
The Details of the Six Real IR Sequences

Sequence	Image Size	Target Size	Target Type	Target Details	Background Details
Real Sequence 1	128 × 128	2 × 2	Airplane	Low SNR value. A dim target. Keeping motionless.	Blurred sea-sky backgrounds. Changing backgrounds.
Real Sequence 2	200 × 256	7 × 7	Small ship	A long imaging distance. Low SNR value. Keeping motionless.	Heavy sea-sky clutter backgrounds. Heavy noise. Changing backgrounds.
Real Sequence 3	200 × 256	4 × 6	Airplane	A long imaging distance. A changing size within a big range. Keeping motion.	Uniform backgrounds to heavy cloudy background.
Real Sequence 4	140 × 256	3 × 5	Airplane	Low SNR value. A small size with a little change. Keeping motionless.	Heavy cloudy clutter backgrounds. Heavy noise. Changing backgrounds.
Real Sequence 5	200 × 256	5 × 5	Aircraft	A long imaging distance. Low SNR value. A dim target. Keeping motion.	Uniform backgrounds. Almost keeping the same.
Real Sequence 6	200 × 256	8 × 8	Airplane	Low SNR value. A small size with a little change. Keeping motionless.	Heavy noise. Changing backgrounds.

TABLE II
The Values of SNR and SNRG of Original images and Filtered Results Obtained Through Different Methods (Real Sequence 1)

	1		2		3		4		5	
	SNR	SNRG	SNR	SNRG	SNR	SNRG	SNR	SNRG	SNR	SNRG
Original	1.7257	0	1.7234	0	1.6889	0	1.6811	0	1.6935	0
LMWIE	19.3830	21.0091	18.7608	20.7375	30.5816	25.1570	13.6138	18.1679	15.5491	19.2582
AGADM	1.6941	–[a]	1.6795	–	1.6725	–	1.6696	–	1.6774	–
MBPM	4.0200	7.3452	4.5945	8.5172	3.9380	7.3533	4.6370	8.8131	3.7171	6.8281
Top hat	9.4453	14.7649	12.1252	16.9462	8.8705	14.4068	10.5176	15.9266	8.1361	13.6325
Our method	65.9963	31.6510	82.3680	33.5876	67.5122	32.0354	93.7901	34.9315	82.9116	33.7964

[a]The "–" mark means the value is negative.

TABLE III
The Values of SNR and SNRG of Original Images and Filtered Results Obtained Through Different Methods (Real Sequence 2)

	1		2		3		4		5	
	SNR	SNRG	SNR	SNRG	SNR	SNRG	SNR	SNRG	SNR	SNRG
Original	5.9441	0	6.1897	0	5.9044	0	6.0097	0	6.3101	0
LMWIE	41.8927	16.9610	39.4010	16.0768	33.4401	15.0619	24.5023	12.2071	40.0449	16.0502
AGADM	5.9142	–[a]	5.9366	–	5.5438	–	6.0612	0.0740	5.7864	–
MBPM	8.0299	2.6124	9.1489	3.3940	7.8702	2.4962	8.1393	2.6347	8.6372	2.7268
Top hat	9.8954	4.4269	12.5721	6.1548	7.9869	2.6241	6.8698	1.1618	8.7593	2.8487
Our method	108.3663	25.2161	119.2842	25.6983	123.3241	26.3975	108.5163	25.1328	119.4381	25.5422

[a]The "–" mark means the value is negative.

respectively, and the details about targets and backgrounds are listed in Table I.

B. Tests on Real Images

Because the highly relevant background components account for most of a small-target IR image and they often distribute in the low-frequency band, the initial and principal work of small-target detection approaches is to suppress complex backgrounds and then enhance small targets. The columns from the second to the sixth in Fig. 5 display the filtered results of five methods before segmentation. Compared to baseline methods, it can be seen that our method has less clutter and residual noise under different clutter backgrounds, which is the key to keep both lower Fa and higher Pd.

For the successive five frame images randomly selected from the six real IR image sequences, the SNRs and SNRGs of the original images and the filtered results obtained through LMWIE, AGADM, and MBPM, top-hat, and our method are listed in Tables II to VII, where the mark "–" means the value is negative. We can find that the SNRs of the original images are low, while the proposed method can improve the SNRs of these images significantly. Tables II to VII show that the improvement of SNR of the AGADM method is faint, and the LMWIE method has a better performance than the other baseline methods for the six real sequences. However, our method can obtain the best performance for all the six real sequences. The same conclusion is also acquired from the comparison of SNRGs. The previously mentioned results show that our method can effectively suppress different

TABLE IV
The Values of SNR and SNRG of Original Images and Filtered Results Obtained Through Different Methods (Real Sequence 3)

	1		2		3		4		5	
	SNR	SNRG	SNR	SNRG	SNR	SNRG	SNR	SNRG	SNR	SNRG
Original	3.4834	0	3.4791	0	3.7902	0	3.6136	0	3.6996	0
LMWIE	20.0670	15.2096	19.8509	15.1263	17.3490	13.2123	13.5804	11.4994	18.1715	13.8248
AGADM	3.1607	–[a]	3.2274	–	3.4443	–	3.3083	–	3.1868	–
MBPM	5.3791	3.7742	6.3870	5.2766	5.6437	3.4582	4.6138	2.1223	4.9575	2.5422
Top hat	15.4788	12.9547	14.5470	12.4261	19.2660	14.1227	19.8937	14.8154	16.7664	13.1257
Our method	87.8956	28.0393	94.8112	28.7079	131.2848	30.7911	76.3879	26.5016	105.1409	29.0724

[a]The "–" mark means the value is negative.

TABLE V
The Values of SNR and SNRG of Original images and Filtered Results Obtained Through Different Methods (Real Sequence 4)

	1		2		3		4		5	
	SNR	SNRG	SNR	SNRG	SNR	SNRG	SNR	SNRG	SNR	SNRG
Original	6.1844	0	6.4482	0	6.6009	0	6.7525	0	6.2722	0
LMWIE	31.0642	14.0193	18.8983	9.3397	18.2581	8.8371	15.9621	7.4725	31.3720	13.9824
AGADM	6.5924	0.5550	6.4023	–	6.4889	–	6.8232	0.0905	6.7666	0.6589
MBPM	5.5496	–[a]	5.8451	–	5.9333	–	5.3750	–	6.2024	–
Top hat	11.3211	5.2518	8.7550	2.6564	7.9493	1.6145	9.8507	3.2801	11.2912	5.3342
Our method	88.7320	23.1357	79.5505	21.8241	96.4762	23.2964	64.9270	19.6593	96.8899	23.7771

[a]The "–" mark means the value is negative.

TABLE VI
The Values of SNR and SNRG of Original images and Filtered Results Obtained Through Different Methods (Real Sequence 5)

	1		2		3		4		5	
	SNR	SNRG	SNR	SNRG	SNR	SNRG	SNR	SNRG	SNR	SNRG
Original	5.5246	0	5.1976	0	6.6767	0	6.0851	0	5.3185	0
LMWIE	70.8295	22.1582	106.0555	26.1947	89.3249	22.5283	83.0476	22.7012	66.4525	21.9344
AGADM	4.0669	–[a]	3.9056	–	4.9911	–	4.8428	–	4.0661	–
MBPM	25.4517	13.2682	18.2918	10.9292	29.6365	12.9454	26.5783	12.8052	22.6227	12.5751
Top hat	36.0846	16.3003	32.1012	15.8144	44.5553	16.4868	41.5249	16.6808	32.1724	15.6339
Our method	140.4497	28.1043	134.5161	28.2595	169.0780	28.0706	128.4551	26.4896	118.5114	26.9594

[a]The "–" mark means the value is negative.

TABLE VII
The Values of SNR and SNRG of Original Images and filtered Results Obtained Through Different Methods (Real Sequence 6)

	1		2		3		4		5	
	SNR	SNRG	SNR	SNRG	SNR	SNRG	SNR	SNRG	SNR	SNRG
Original	7.3498	0	5.8740	0	6.1031	0	6.5540	0	7.6387	0
LMWIE	35.6744	13.7216	21.9195	11.4379	53.1745	18.8031	30.5446	13.3685	21.0456	8.8028
AGADM	6.2102	–[a]	5.4629	–	5.9720	–	6.1934	–	6.5356	–
MBPM	8.5026	1.2655	6.4652	0.8329	7.9776	2.3266	7.2712	0.9020	9.0385	1.4615
Top hat	12.1209	4.3451	8.8366	3.5470	13.8963	7.1470	10.1932	3.8360	10.6600	2.8947
Our method	132.2863	25.1047	127.9320	26.7609	126.9575	26.3622	135.9599	26.3381	147.2130	25.6985

[a]The "–" mark means the value is negative.

clutters and noise backgrounds and then enhance small targets.

The position of the target alters in each frame of both Real Sequence 3 and Real Sequence 5 (see Table I), while the targets in Real Sequences 1, 2, 4, and 6 keep motionless. The trajectory and error curve of the first 30 consecutive frames of Real Sequences 3 and 5 are shown in Figs. 6a, 6b, respectively. In Fig. 6a, the tracking trace does almost match that of the target movement. From the lower panels of Fig. 6a, we observe that the horizontal error is less than 1 pixel, and the vertical error is less than 1.5 pixels. For Real Sequence 5, the tracking trace also

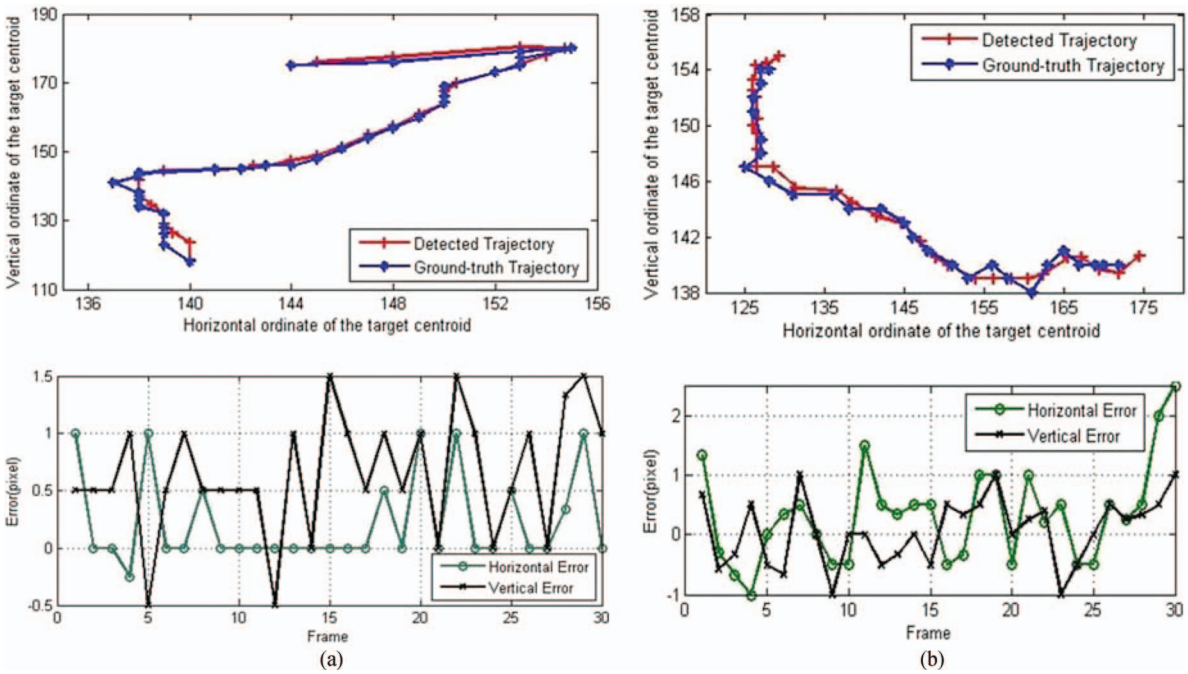

Fig. 6. Detected trajectories (upper) and corresponding detected errors (lower). (a) Detected results of first 30 frames of Real Sequence 3. (b) Detected results of first 30 frames of Real Sequence 5.

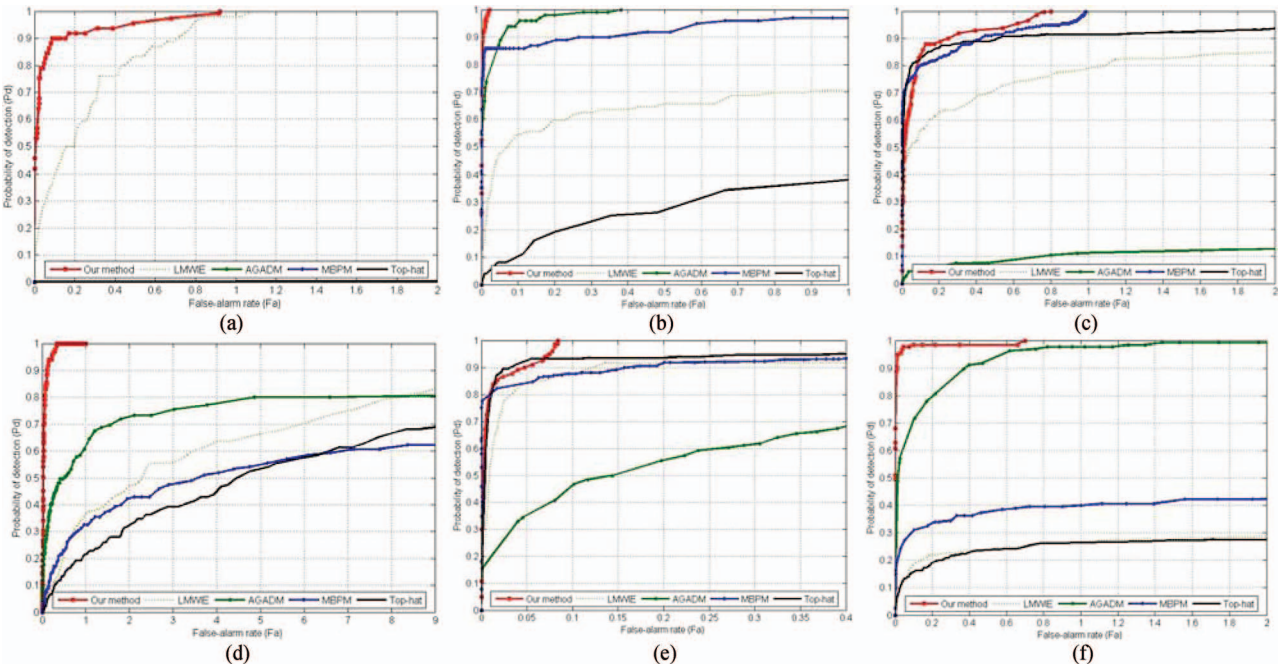

Fig. 7. ROC curves of five methods for six real image sequences. (a) Real Sequence 1. (b) Real sequence 2. (c) Real Sequence 3. (d) Real Sequence 4. (e) Real Sequence 5. (f) Real Sequence 6.

does almost match that of the target movement, the vertical error shown in Fig. 6b is less than 1 pixel, and the horizontal error is less than 2.5 pixels. Usually, if the distance between centers of the ground truth and the detected result is within a threshold, then the detection is admitted as being correct [11, 23]. The threshold in [23] is chosen as 5 pixels, while in [1], it is 4 pixels. In this paper, the threshold is selected as 3 pixels. The smaller threshold chosen suggests less errors between the ground truth and the detected results. Consequently, it demonstrates that the proposed method is very effective.

Fig. 7 shows the receiver operating characteristic (ROC) curves of the five methods for six real image sequences. Our method has better performance than baseline methods, especially for Real Sequence 1, 2, 4, and 6, the proposed method owns higher Pds but lower Fas, compared with the baseline methods. For Real Sequence 1, the AGADM method, MBPM method, and

top-hat method have very low values of Pd when Fa ≤ 2. For Real Sequence 3, the MBPM method and top-hat method have a little better performance than our method when Fa ≤ 0.1, but our method can reach 1 (100%) faster than these baseline methods when Fa > 0.1. The similar results can be obtained from Real Sequence 5, too. Fig. 7 also shows that the AGADM method has better performance than other baseline methods for Real Sequences 2, 4, and 6. In addition, the heavy cloud edge texture and heavy noise (Real Sequence 4) have an effect on the performance of our method. However, our method can obtain the best performance for all six real IR sequences, which implies that our method works more robustly for various clutter and noisy backgrounds, target types, and target movements.

V. CONCLUSION

An effective IR small-target detection method is presented based on the NWIE in this paper. The method weights the local entropy measure by the multiscale grayscale difference followed by an adaptive threshold operation that aims to improve the SNR for cases in which jamming objects (e.g., the edge of clouds) in the scene have a similar thermal intensity measure wrt the background as a small target. It can suppress different clutter and noisy backgrounds and enhance the targets simultaneously, especially in the improvement of SNR. Extensive real data experiments demonstrate that the proposed method significantly outperforms the conventional baseline methods, such as the LMWIE, AGADM, MBPM, and top-hat methods, and it demonstrates that the proposed novel method works robustly for different clutter and noisy backgrounds, target types, and target movements. Although the experiment results suggest that the proposed method is efficient and they provide empirical evidence to support the conclusion that it is suitable to detect IR small targets, we will keep improving it from different directions in future work. For example, we will improve the flexibility of the method in background cases with heavy interference of the cloud edge texture and noise.

REFERENCES

[1] Gao, C. Q., Meng, D. Y., Yang, Y., Wang, Y. T., Zhou, X. F., Hauptmann, A. G.
Infrared patch-image model for small target detection in a single image.
IEEE Transactions on Image Processing, **22**, 12 (Dec. 2013), 4996–5009.

[2] Porat, B., and Friendlander, B.
A frequency domain algorithm for multi-frame detection and estimation of dim targets.
IEEE Transactions on Pattern Analysis and Machine Intelligence, **12**, 4 (Apr. 1990), 398–401.

[3] Bai, X. Z., and Zhou, F. G.
Analysis of new top-hat transformation and the application for infrared dim small target detection.
Pattern Recognition, **43**, 6 (June 2010), 2145–2156.

[4] Deng, H., Wei, Y. T., and Tong, M. W.
Small target detection based on weighted self-information map.
Infrared Physics & Technology, **60** (Sep. 2013), 197–206.

[5] Gao, C. Q., Zhang, T. Q., and Li, Q.
Small infrared target detection using sparse ring representation.
IEEE Aerospace and Electronic Systems Magazine, **27**, 3 (Mar. 2012), 21–30.

[6] Reed, I. S., Gagliardi, R. M., and Stotts, L. B.
Optical moving target detection with 3-D matched filtering.
IEEE Transactions on Aerospace and Electronic Systems, **24**, 4 (July 1988), 327–336.

[7] Li, M., Zhang, T., Yang, W., and Sun, X.
Moving weak point target detection and estimation with three-dimensional double directional filter in IR cluttered background.
Optical Engineering, **44** (Oct. 2005), 107007.

[8] Liu, X., and Zuo, Z.
A dim small infrared moving target detection algorithm based on improved three-dimensional directional filtering communications in computer and information science.
In Advances in Image and Graphics Technologies, Vol. 363. New York: Springer-Verlag, 2013, ch. 13, 102–108.

[9] Pohlig, S. C.
Spatial-temporal detection of electro-optic moving targets.
IEEE Transactions Aerospace and Electronic Systems, **31**, 2 (Apr. 1995), 608–616.

[10] Deshpande, S. D., Er, M. H., and Venkateswarlu, R.
Max-mean and max-median filters for detection of small-targets.
Proceedings of SPIE, **3809** (Oct. 1999), 74–83.

[11] Kim, S., and Lee, J.
Scale invariant small target detection by optimizing signal-to-clutter ratio in heterogeneous background for infrared search and track.
Pattern Recognition, **45**, 1 (Jan. 2012), 393–406.

[12] Yang, L., Yang, J., and Yang, K.
Adaptive detection for infrared small target under sea-sky complex background.
Electronics Letters, **40**, 17 (Aug. 2004), 1083–1085.

[13] Strickland, R. N., and Hahn, H. I.
Wavelet transform methods for objects detection and recovery.
IEEE Transactions on Image Processing, **6**, 5 (May 1997), 724–735.

[14] Deng, H., Liu, J. G., and Chen, Z.
Infrared small target detection based on modified local entropy and EMD.
Chinese Optics Letters, **8**, 1 (Jan. 2010), 24–28.

[15] Kim, S., and Lee, J.
Small infrared target detection by region-adaptive clutter rejection for sea-based infrared search and track.
Sensors (Basel), **14**, 7 (July 2014), 13210–13242.

[16] Khan, J. F., and Alam, M. S.
Target detection in cluttered forward-looking infrared imagery.
Optical Engineering, **44**, 7 (July 2005), 076404.

[17] Shirvaikar, M., and Trivedi, M.
A neural network filter to detection small targets in high clutter backgrounds.
IEEE Transactions on Neural Networks, **6**, 1 (Jan. 1995), 252–257.

[18] Li, H., Wei, Y., Li, L., and Tang, Y. Y.
Infrared moving target detection and tracking based on tensor locality preserving projection.
Infrared Physics & Technology, **53**, 2 (Mar. 2010), 77–83.

[19] Wang, Z., Tian, J., Liu, J., and Zhen, S.
Small infrared target fusion detection based on support vector machines in the wavelet domain.
Optical Engineering, **45**, 7 (July 2006), 76401.

[20] Gu, Y. F., Wang, C., Liu, B. X., and Zhang, Y.
A kernel-based nonparametric regression method for clutter removal in infrared small-target detection application.
IEEE Geoscience and Remote Sensing Letters, **7**, 3 (July 2010), 469–473.

[21] Deng, H., Liu, J. G., and Li, H.
EMD based infrared image target detection method.
Journal of Infrared Millimeter, and Terahertz Waves, **30**, 11 (Jul. 2009), 1205–1215.

[22] Shui, P. L., Li, D. C., and Xu, S. W.
Tri-feature-based detection of floating small targets in sea clutter.
IEEE Transactions on Aerospace and Electronic Systems, **50**, 2 (Apr. 2014), 1416–1430.

[23] Philip, C. L., Li, H., Wei, Y. T., Xia, T., and Tang, Y. Y.
A local contrast method for small infrared target detection.
IEEE Transactions on Geoscience Remote Sensing, **52**, 1 (Jan. 2014), 574–581.

[24] Song, D., and Tao, D.
Biologically inspired feature manifold for scene classification.
IEEE Transactions on Image Processing, **19**, 1 (Jan. 2010), 174–184.

[25] Rivest, J. F., and Fortin, R.
Detection of dim targets in digital infrared imagery by morphological image processing.
Optical Engineering, **35**, 7 (July 1996), 1886–1893.

[26] Anderson, K. L., and Iltis, R. A.
A tracking algorithm for infrared images based on reduced sufficient statistics.
IEEE Transactions on Aerospace and Electronic Systems, **33**, 2 (Apr. 1997), 464–472.

[27] Qu, X. J., Chen, H., and Peng, G. H.
Novel detection method for infrared small targets using weighted information entropy.
Journal of Systems Engineering and Electronics, **23**, 6 (Dec. 2012), 838–842.

[28] Deng, H., Wei, Y. T., and Tong, M. W.
Background suppression of small target image based on fast local reverse entropy operator.
IET Computer Vision, **7**, 5 (Oct 2013), 405–413.

[29] Wang, G. Y., Zhang, T. X., Wei, L. G., and Sang, N.
Efficient method for multiscale small target detection from a natural scene.
Optical Engineering, **35**, 3 (Mar. 1996), 761–768.

[30] Tsai, D. Y., Lee, Y., and Matsuyama, E.
Information entropy measure for evaluation of image quality.
Journal of Digital Imaging, **21**, 3 (Sep. 2008), 338–347.

[31] Pal, N. R., and Pal, S. K.
Entropy: a new definition and its application.
IEEE Transactions on Systems, Man and Cybernetics, **21**, 5 (Sep. 1991), 1260–1270.

[32] Victor, J. D., and Conte, M. M.
Local image statistics: maximum-entropy constructions and perceptual salience.
Journal of the Optical Society of America A: Optics, Image Science, and Vision, **29**, 7 (July 2012), 1313–1345.

[33] Tom, V., Peli, T., Leung, M., and Bondaryk, J.
Morphology-based algorithm for point target detection in infrared backgrounds.
Proceedings of SPIE, **1954** (Oct. 1993), 25–32.

[34] Toet, A., and Wu, T.
Small maritime target detection through false color fusion.
Proceedings of SPIE, **6945** (Apr. 2008), 69450V–69453V.

[35] Huang, K., and Mao, X.
Detectability of infrared small targets.
Infrared Physics & Technology, **53**, 3 (May 2010), 208–217.

He Deng received his Ph.D. degree in control science and engineering from Huazhong University of Science and Technology in 2011. Now, he is a postdoctoral researcher at the Wuhan Institute of Physics and Mathematics, Chinese Academy of Sciences, and he is a lecturer in the Department of Information Technology at Central China Normal University. His current research interests are target detection and image processing.

Xianping Sun received his B.S. degree from Peking University in 1980. Now, he is a professor at the Wuhan Institute of Physics and Mathematics, Chinese Academy of Sciences. His current research interests include signal acquisition and processing.

Maili Liu received his Ph.D. degree from University of London in 1996. Now, he is a professor at the Wuhan Institute of Physics and Mathematics, Chinese Academy of Sciences. His current research interests include nuclear magnetic resonance spectroscopy, imaging acquisition, and applications.

Chaohui Ye received his B.S. degree from Peking University in 1965. Now, he is a professor at the Wuhan Institute of Physics and Mathematics, Chinese Academy of Sciences. His current research interests include novel imaging techniques and applications in biomedicine and physics.

Xin Zhou received his Ph.D. degree from the Chinese Academy of Sciences in 2004. Now, he is a professor at the Wuhan Institute of Physics and Mathematics, Chinese Academy of Sciences. His current research interests are scientific instrument developments, imaging acquisition, and data processing.